# Cascaded Thinning in Upscale and Downscale Representation for EEG Signal Processing

Quang Manh Doan, Tran Hiep Dinh, *Member, IEEE*, Avinash Kumar Singh, *Member, IEEE*, Chin-Teng Lin, *Fellow, IEEE*, and Nguyen Linh Trung, *Senior Member, IEEE*

***Abstract*— Smoothing filters are widely used in EEG signal processing for noise removal while preserving signals' features. Inspired by our recent work on Upscale and Downscale Representation (UDR), this paper proposes a cascade arrangement of some effective image-processing techniques for signal filtering in the image domain. The UDR concept is to visualize EEG signals at an appropriate line width and convert it to a binary image. The smoothing process is then conducted by skeletonizing the signal object to a unit width and projecting it back to the time domain. Two successive UDRs could result in a better-smoothing performance, but their binary image conversion should be restricted. The process is computationally ineffective, especially at higher line width values. Cascaded Thinning UDR (CTUDR) is proposed, exploiting morphological operations to perform a two-stage upscale and downscale within one binary image representation. CTUDR is verified on a signal smoothing and classification task and compared with conventional techniques, such as the Moving Average, the Binomial, the Median, and the Savitzky Golay filters. Simulated EEG data with added white Gaussian noise is employed in the former, while cognitive conflict data obtained from a 3D object selection task is utilized in the latter. CTUDR outperforms its counterparts, scoring the best fitting error and correlation coefficient in signal smoothing while achieving the highest gain in Accuracy (0.7640%) and F-measure (0.7607%) when used as a smoothing filter for training data of EEGNet.**

Received 13 September 2023; revised 2 June 2024 and 7 August 2024; accepted 10 September 2024. Date of publication 25 September 2024; date of current version 7 October 2024. This research was funded by the research project QG (QG.23.35) of Vietnam National University, Hanoi. The work of Avinash Kumar Singh and Chin-Teng Lin was supported in part by the Australian Research Council (ARC) under discovery grant DP210101093 and DP220100803, and in part by the Australian National Health and Medical Research Council (NHMRC) under Ideas Grant APP2021183. An earlier version of this paper was presented at the 2023 IEEE Statistical Signal Processing Workshop (SSP) [DOI: 10.1109/SSP53291.2023.10207993]. *(Corresponding author: Tran Hiep Dinh.)*

This work involved human subjects in its research. Approval of all ethical and experimental procedures and protocols was granted by the Ethics Committees of the University of Technology Sydney, Australia.

Quang Manh Doan and Nguyen Linh Trung are with the Advanced Institute of Engineering and Technology (AVITECH), VNU University of Engineering and Technology, Hanoi 10000, Vietnam (e-mail: mdq@vnu.edu.vn; linhtrung@vnu.edu.vn).

Tran Hiep Dinh is with the Faculty of Engineering Mechanics and Automation, VNU University of Engineering and Technology, Hanoi 10000, Vietnam (e-mail: tranhiep.dinh@vnu.edu.vn).

Avinash Kumar Singh and Chin-Teng Lin are with Australian Artificial Intelligence Institute, School of Computer Science, Faculty of Engineering and Information Technology, University of Technology Sydney, Sydney, NSW 2007, Australia (e-mail: avinash.singh@uts.edu.au; chin-teng.lin@uts.edu.au).

Digital Object Identifier 10.1109/TNSRE.2024.3465515

***Index Terms*— Smoothing, thinning, skeletonization, electroen-cephalogram (EEG), signal processing, time-series, noise, filter.**

## I. Introduction

ELECTROENCEPHALOGRAM (EEG) is widely used for clinical diagnosis and monitoring to detect brain disorders [1], [2] as well as in Brain-Computer Interface (BCI) applications [3], [4]. One of common practices in EEG signal processing for specific pattern detection is via the visual inspection and interpretation of neurologists [5]. As EEG signals are impacted by noise, smoothing filters are required to increase the signal-to-noise ratio and preserve neural information [6]. Smoothing filters highlight temporal trends, aiding in identifying neural patterns related to cognition, disorders, and brain states, thus enhancing analysis accuracy, advancing our understanding of brain function, and guiding clinical decisions [7], [8]. Therefore, the higher the EEG signal quality, the more promising results can be expected. Hence, EEG signal noise reduction becomes a vital aspect of EEG signal processing.

Many fields of engineering and science can benefit from the use of smoothing filters [9], [10], including computer vision [11], signal processing [12], and time series analysis [9], [13], [14], [15], [16]. EEG signal processing is no exception when numerous smoothing filters are developed to reduce noise in EEG signals. Some conventional filters applied to EEG signal smoothing are Moving Average, Savitzky-Golay [17], and Binomial Filter [18]. Unlike these algorithms that filter out the signal in the time domain, a recent effective approach in image domain, UDR [19], has been proposed. The concept behind UDR is to visualize the input signal at a suitable line width and convert it to a binary image. After that, the signal object is skeletonized to a unit width and projected back into the time domain. The quantitive results in [19] have shown the promising capability of UDR on noise removal in EEG signals.

It has been pointed out in [20] that a successive two-stage filter can significantly increase the smoothing results. Cascade arrangements have been implemented widely to increase filter and model effectiveness. For instance, a two-stage methodology using a fuzzy weighted mean and fractional integration filter has been proposed in [21] to perform image denoising. A cascaded spatio-temporal processing procedure (CAST) is

developed to remove artifact electrooculogram (EOG) in [22]. Besides, cascaded filters are also employed in pre-processing to enhance data quality. For example, the raw lung sound signals are filtered using an IIR Butterworth band pass filter and then passed through four cascaded notch filters to remove the power line noise as in [23]. A cascaded arrangement is applied in a classification model in [24] to extract features and classify heartbeats in order to improve the performance of ECG beat classification via multi-lead ECG. In our preliminary work on using a cascade arrangement on UDR, hence the name CUDR [25], the effectiveness of a straightforward cascade arrangement of UDR has been verified in terms of noisy signal smoothing.

As UDR was developed in the image domain, some image-processing techniques can potentially enhance the UDR and CUDR performance. Hence comes an alternative arrangement, the cascaded thinning UDR approach. CUDR consists of two processing stages of UDR, where the output of the former is the input of the latter with a different line width. A signal is required to be visualized, converted to the image domain, and projected back to the time domain twice, resulting in a computationally inefficient solution. To overcome this limitation, we propose here the CTUDR approach, reducing the visualization steps while leveraging the scale-changing mechanism. The processing steps in CUDR are improved in CTUDR, where the signal object is first filtered with some morphological operators, then skeletonized and eventually projected to the time domain to achieve the smoothed signal. By combining morphological operations and skeletonization, the signal object in the binary image is enlarged and shrunk twice. This approach allows the perseverance of the outperformance of the smoothing via skeletonization while bypassing the double representation in CUDR. Two datasets are utilized in this work to verify the effectiveness of CTUDR in the signal smoothing and classification tasks: (i) a simulated dataset comprising 5040 signals generated from seven components and (ii) a real EEG dataset used for Cognitive Conflict (CC) analysis [26], [27]. The CC dataset was obtained from experiments involving 33 participants who engaged in a 3D object selection task in a virtual reality (VR) environment. Compared with our preliminary work on CUDR [25], the following have been extended: i) development of CTUDR with better performance in accuracy and processing time, ii) experiments of CUDR and CTUDR on real EEG data, and iii) parameter optimization of CTUDR. The contributions of this work include:

- a cascade thinning framework, CTUDR, with significant improvements in both signal smoothing and cognitive conflict classification,
- comprehensive experiments on simulated and cognitive conflict data as well as detailed analysis on the impact of structuring elements on the proposed approach's performance.

The rest of the paper is structured as follows: the overview of UDR, the idea of CUDR and CTUDR are described in Section II. The data and evaluation metrics used in this work are declared in Section III. The results of the extended UDR and some comparative smoothing filters are reported in Section IV. The discussion and conclusion are presented respectively in Sections VI and VII.

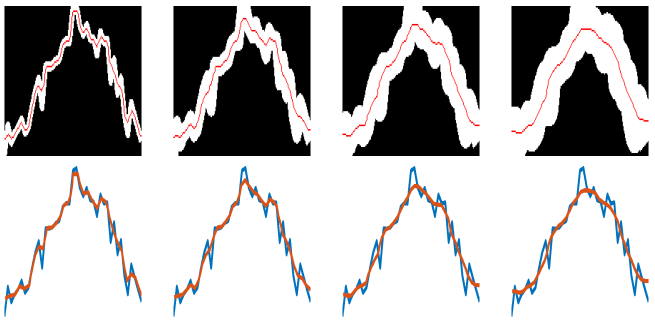

(a) $W = 5$ (b) $W = 10$ (c) $W = 15$ (d) $W = 20$

Fig. 1. Representation of a signal segment in binary images and corresponding correlations between their skeletonizations and original samples.

## II. Methodology

### A. Image Processing Techniques Used in CTUDR

In this section, some common terms and techniques used in the processing of CTUDR as well as other filters in the UDR filter family (UDR [19], CUDR [25]) are introduced, including line width, skeletonization, erosion, and dilation. Line width $W$ is a parameter that identifies the thickness of the signal curve when represented in the image domain. Fig. 1 demonstrates the representation of a signal segment in the image domain at different line width values (first row), i.e. $W = \{5, 10, 15, 20\}$, and the corresponding correlation of its skeleton with the original signal in the time domain (second row). The original and smoothed signals are represented in blue and orange, while the signal representation in binary images is white. The signal segment consists of a dominant peak with minor ones on both sides. At higher line width values, minor peaks are represented by overlapped white pixels and disappear when being skeletonized.

Skeletonization is an image processing technique that reduces the thickness of shapes within an image to their essential structure, often resembling a skeleton [28]. It iteratively removes the shapes' border pixels until they become single-pixel lines with preserved connectivity and topology [29]. Let us denote $BW$ as a 2-D binary array sized $m \times n$, representing the signal of interest in the image domain. $BW$ contains a nonempty subset $S$ of 1s pixels representing the signal shape and a complementary subset $\bar{S}$ of 0s pixels representing the background. According to [29], the border pixel $v = (x, y)((x, y) < (m, n))$ within a 8-neighborhood $N(v)$ is identified as

$$\delta O(S \cap N(v)) = 0, \tag{1}$$

where $O(S)$, $H(S)$, and $C(S)$ are the counts of connected objects, holes, and cavities of $S$, $\delta$ is the change of the Euler characteristics $\chi(S)$, which is calculated as

$$\chi(S) = O(S) - H(S) + C(S). \tag{2}$$

Erosion and dilation are morphological operations using translated or reflected structuring elements to thin or thicken

objects in an image [30]. Let $SE$ be the employed structuring element; its by-point-$z$ translation $(SE)_z$ and reflection $\hat{SE}$ are defined as

$$(SE)_z = \{c | c = u + z, \text{ for } u \in SE\}, \tag{3}$$

$$\hat{SE} = \{w | w = -u, \text{ for } u \in SE\}. \tag{4}$$

The erosion operation, denoted as $BW \ominus SE$, is to find a set of pixels in $BW$ to place the origin of $SE$ so that it is completely contained in $BW$, i.e.

$$BW \ominus SE = \{z | (SE)_z \subseteq BW)\}. \tag{5}$$

This mechanism allows the removal of border pixels in $BW$, since the placement of $SE$'s origin in these locations does not result in a full overlap between $BW$ and $SE$.

The dilation operation, denoted as $BW \oplus SE$, is to find a set of pixels in $BW$ to place the origin of $\hat{SE}$ so that there is at least one overlapping pixel between $BW$ and $\hat{SE}$. At each found placement, the origin of $\hat{SE}$ is added to $BW$, resulting in an expansion of the original shape. The operation is defined as

$$BW \oplus SE = \{z | [(\hat{SE})_z \cap BW] \subseteq BW\}. \tag{6}$$

Erosion and dilation not only allow the shrinking and thickening of objects in a binary image but also can be combined to remove unwanted pixels or reduce disparity. Hence, these operators are employed in this work to develop CTUDR.

### B. Overview on UDR and CUDR

*1) UDR:* The idea of upscaling in UDR is inspired by the "zoom in" process when neurologists visually inspect signals for peak labeling on EEG peak detection in cognitive conflict processing [26], [31]. Let $X$ be the signal to be processed, $W$, and $T_W$ be the line width of the plotted signal and the line width threshold value, respectively. The noisy signal is first graphically visualized with the initial line width $W$ in a figure. Then, the figure is converted into a binary image. A unit-width curve representing the signal is generated from the binary image by applying a thinning algorithm. Finally, the skeletonized curve is projected back to time domain. As reported in [19], UDR outperforms other conventional filters in the noise removal of simulated data task. Besides, the experiment on a real EEG dataset also shows promising results in a signal classification task.

A disadvantage of UDR is its high computation requirement. Indeed, UDR must adjust line width W until the correlation is maximum. With different signal durations, UDR requires a parameter set that generates the best-smoothed signal. As per our observation, UDR using a low line width can result in a waveform similar to the original signal with some unwanted noise. Although using a thicker line width can return a smoother skeleton, the waveform of which is flatter where some peaks are not preserved. Therefore, CUDR [25] is proposed where a low $W$ is implemented in the initial stage for waveform perseverance and a high $W$ is employed in the second stage for signal smoothing. The idea is presented in Section II.B and verified in Section IV.

**Algorithm 1** CTUDR

**Input:** $X, W, SE$
**Output:** $Y$

```
i ← 1
Plot X at W_i
Obtain BW_o as per Eq. 7
while i ≥ 1 do
    Skel ← skeletonize BW_o
    i++
    if i > 2 then
        break
    end if
    dilate Skel to W_i
end while
Y ← project Skel back to time domain
```

*2) CUDR:* The two-stage or cascaded Savitzky-Golay smoothing filter (CSG) for biomedical signal processing is introduced in [20] to reduce signal distortion. As reported in [20], CSG worked better in signal denoising compared to other filters: Cascaded Moving Average (CMA), Cascaded Savitzky-Golay with Moving Average (CSGMA), Cascaded Savitzky-Golay with Binomial filter (CSGB) and single-stage Savitzky-Golay (SG), even in very noisy level (SNR $= -5$dB). Inspired by the ideas in [19] and [20], a cascaded arrangement of UDR is developed in this work to verify its performance in signal smoothing. Here, the input signal is filtered by going through successive UDRs using different line width values at each stage.

In UDR, the skeleton generated from the binary image is impacted by the level of the signal noise. Fig. 2(a) and 2(b) illustrate the binary image of a generated signal epoch and an extremely noisy signal by adding noise to the original generated one, respectively. Fig. 2(c) illustrates the binary image of UDR skeletonization in the noisy signal epoch, the skeleton of which consists of unwanted branches. This branch issue can be removed by using an appropriate thinning threshold, or increase the line width $W$. Both approaches require human intervention and limit the automation of the algorithm, yet to mention the additional computational burden. Fig. 2(d) illustrates the effectiveness of UDR at higher value of $W$, although the processing time is also increased in this case. Here, a cascade arrangement of UDR is proposed where the input signal is processed through two successive stages with different line width values $W$. The input signal is first represented at a lower $W$ and smoothed in the former, the result of which is then represented at a higher $W$ and smoothed in the latter. Fig. 2(e) illustrates the result of the proposed CUDR where the line width values are correspondingly selected as 10 and 25 at the first and second stages. It can be seen that the waveform is well preserved while the line width is not required to reach 30 as shown in Fig. 2(d) to reach a desired performance.

### C. CTUDR

As introduced above, the visualization of the object signal in the binary image using two different representation frames

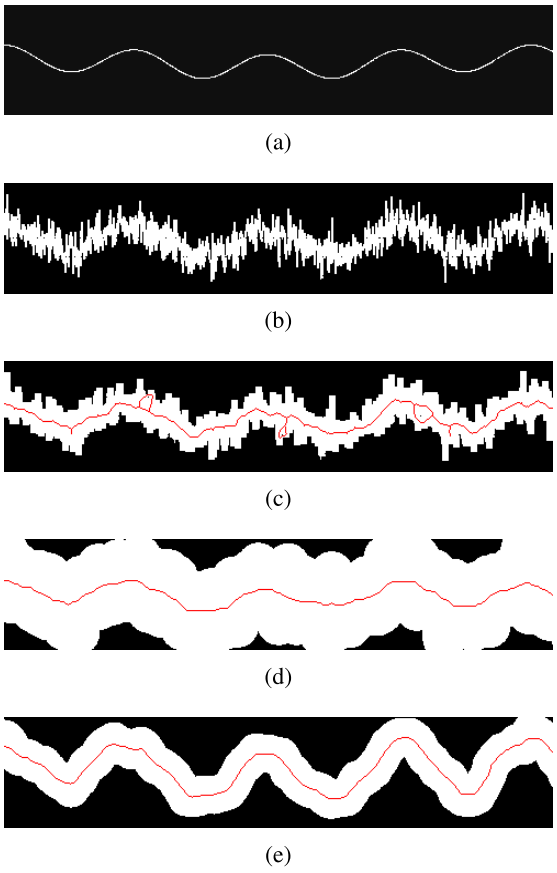


Fig. 2. Skeletonization on a signal using UDR and CUDR (plotted signal and corresponding skeleton are respectively represented in white and red): (a) Original signal, (b) Noisy signal, (c) UDR ($W = 5$), (d) UDR ($W = 30$), and (e) CUDR ($W_1 = 10$ and $W_2 = 25$).

results in a slower processing time of CUDR. To deal with this limitation, in this work, some morphological operators are utilized to successively conduct the enlargement and thinning process without exploiting the visualization.

Fig. 3(a) shows the processing pipeline of CUDR where the binary image representation is looped and represented larger than other blocks, emphasizing its high computational cost compared to that of the others. The pipeline structure is simplified in CTUDR, as shown in Fig. 3(b), where the binary image representation is placed out of the loop and the combination between thinning and morphological operations is leveraged. After converting the figure representing the signal to a binary image, image erosion and dilation are implemented. The purpose of the erosion step is to avoid unwanted branches that might appear in the skeletonization. Dilation is then applied to reduce the potential object disparity resulting from erosion. Let $BW$ be the binary image representation of the signal at $W_i$, its morphological opening $BW_o$ by a structuring element $SE$ is defined as

$$BW_o = (BW \ominus SE) \oplus SE. \tag{7}$$

Similar to the first stage of CUDR, the resulting object is thinned to obtain the skeleton. This skeleton is then dilated to a larger scale, then thinned again and projected back to the time domain. The selection of the structuring elements to optimize the performance of CTUDR is analyzed in Section V. With this mechanism, the input signal is represented at two different scales without being visualized twice as per the CUDR, leading to a potential reduction in processing time. The pseudo-code of CTUDR is presented in Algorithm 1.

Fig. 4 demonstrates the immediate results of CTUDR's processing steps on a test signal under the effect of white Gaussian noise, the level of which is SNR $= -1$ dB. Notably, the smoothness of the object is increased after each cycle of dilation and skeletonization.

## III. Data and Evaluation Metrics

### A. Data

*1) Simulated Data:* Let $P_i$, $P_s$ be respectively the power of an input signal I and the noise S when I is added to a white Gaussian noise n. The signal-to-noise ratio ($SNR$) is defined as

$$SNR = \frac{P_i}{P_s}. \tag{8}$$

In this work, a multi-component signal dataset is generated to evaluate the enhancement of the proposed algorithm compared to UDR. Each component is defined as

$$X(t) = I(t) + n(t), \tag{9}$$

where n(t) is white Gaussian noise at SNR of $-15$, $-10$, $-5$, $-1$, and 1 dB, and $I(t)$ is the synthetic signal as introduced in [32]. There are seven signal components which are described as follows:

Component 1:

$$I_1(t) = 0.5\cos(\pi t) + 1.5\cos(4\pi t) + 4\cos(5\pi t). \tag{10}$$

Component 2:

$$I_2(t) = 0.7\cos(\pi t) + 2.1\cos(4\pi t) + 5.6\cos(5\pi t). \tag{11}$$

Component 3:

$$I_3(t) = 1.5\cos(2\pi t) + 4\cos(8\pi t). \tag{12}$$

Component 4:

$$I_4(t) = 1.5\cos(\pi t) + 4\cos(4\pi t). \tag{13}$$

Component 5:

$$I_5(t) = 0.5\cos(\pi t) + 1.5\cos(2\pi t) + 0.8\cos(3\pi t) + 3.5\cos(5\pi t). \tag{14}$$

Component 6:

$$I_6(t) = 4.5\cos(3\pi t) + 2.2\cos(5\pi t). \tag{15}$$

Component 7:

$$I_7(t) = 0.8\cos(\pi t) + \cos(3\pi t) + 3\cos(5\pi t). \tag{16}$$

Then, all seven signal components are joined in random order and duration from 2.75 to 4 s. In this work, 5040 concatenated signals were generated based on all cases of seven components permutation used as a dataset for evaluation. In reality, an EEG signal also has different waves at different amplitudes and

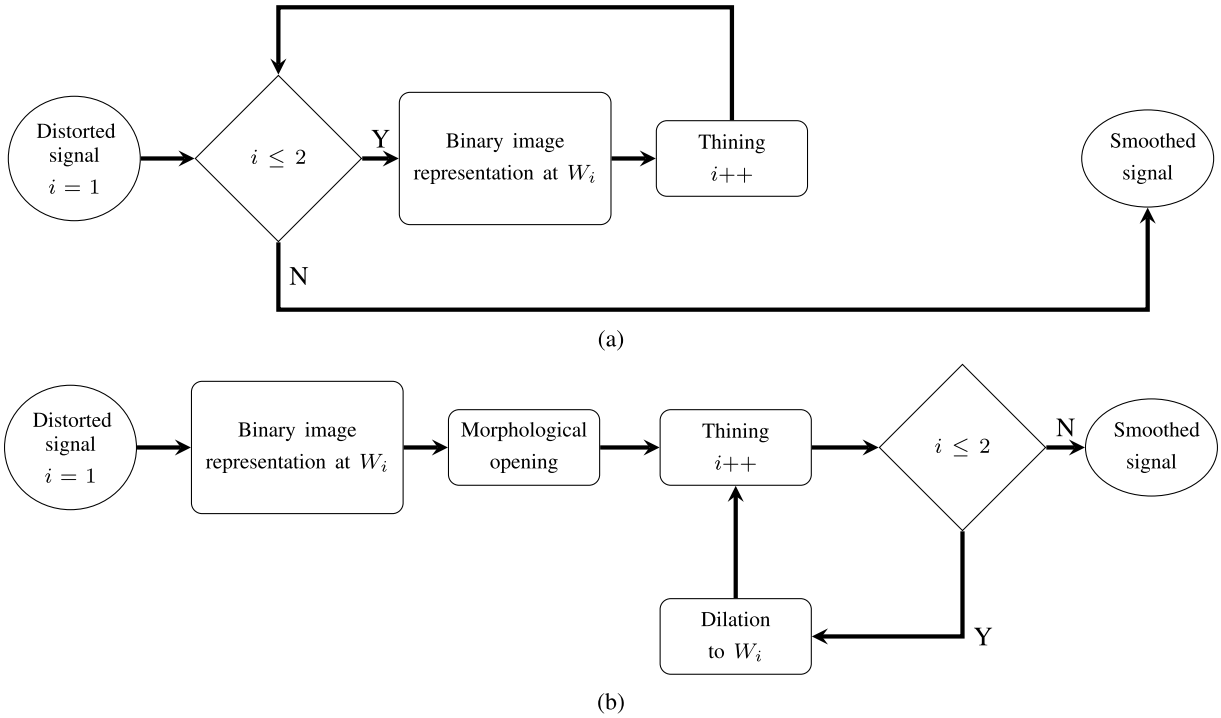


Fig. 3. Processing pipeline of a) CUDR and b) CTUDR.

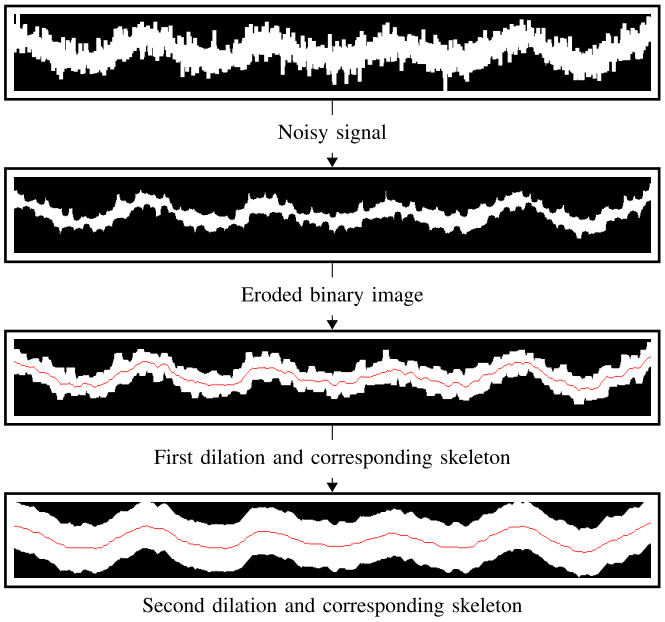


Fig. 4. Demonstration of the CTUDR progress.

frequencies, so with this arrangement, the concatenated signals generated still keep vital characteristics of the real-EEG signal [20]. The simulated dataset is generated using MATLAB R2021b.

*2) Real EEG Data:* In this experiment, real EEG data from our co-authors' study in cognitive conflict processing is employed. Cognitive conflict is a reaction of the human brain when a stimulus unexpectedly appears in ongoing action. In this work, the Cognitive Conflict dataset (CC), collected from experiments of 33 participants who performed the 3D object selection task in a virtual reality (VR) environment [26], [27], is employed to compare the effectiveness of comparative algorithms in classification and visual inspection tasks. As reported in [33], when cognitive conflict occurs, in the time window from 50 to 150ms and 250 to 350ms, a prediction error negativity (PEN) and an error-related positive potential (Pe), respectively, can be seen in event-related potential (ERP) of EEG signals. To deal with the classification task, this EEG dataset with dimension 62 channels $\times$ 1200 datapoints $\times$ 3532 epochs are utilized, where the samples are split equally into two classes: conflict and non-conflict, the latter condition does not show PEN in ERP. Then, CUDR and CTUDR are evaluated by employing a widely-used deep learning model, EEGNet [34], on the CC dataset using these smoothing filters in the classification task.

## B. Evaluation Metrics

Let $I$ and $Y$ are respectively the input and ouput signals, the Root Mean Square Error (*RMSE*) and the Correlation Coefficient (*COR*) evaluating the signal correlation are defined as

$$RMSE = \sqrt{\frac{\sum_{k=1}^{N}(I_k - Y_k)^2}{N}}. \tag{17}$$

$$COR = \frac{1}{N-1}\sum_{k=1}^{N}\left(\frac{I_k - \mu_I}{\sigma_I}\right)\left(\frac{Y_k - \mu_Y}{\sigma_Y}\right), \tag{18}$$

where $\mu$ and $\sigma$ are the mean and standard deviation of the signal, $N$ is the number of data points in the observed interval.

For each concatenated signal $I(t)$ at a specific noise level, a noise signal is randomly generated by adding white Gaussian noise to the $I(t)$ called $X(t)$. The *RMSE* and *COR* between

TABLE I
COMPARATIVE FILTERS

| Filters | Order | Span/ Binomial coeficients |
|---|---|---|
| Moving average (*MA5*) [8] | N/A | 5 |
| Moving average (*MA15*) [8] | N/A | 15 |
| Savitzky-Golay (*SG2*) [8] | 2 | 5 |
| Savitzky-Golay (*SG4*) [8] | 4 | 27 |
| Median Filter (*MF*) [8] | 9 | N/A |
| Bionomial Filter (*BF*) [20] | N/A | 21 |
| Savitzky-Golay (*SG8*) [20] | 8 | 21 |
| Moving average (*MA21*) [20] | N/A | 21 |
| **Cascaded Filters** | **Stage 1** | **Stage 2** |
| *CMA5* | *MA5* | *MA5* |
| *CMA15* | *MA15* | *MA15* |
| *CSG2* | *SG2* | *SG2* |
| *CSG4* | *SG4* | *SG4* |
| *CMF* | *MF* | *MF* |
| *CSG8-BF* [20] | *SG8* | *BF* |
| *CSG8* [20] | *SG8* | *SG8* |
| *CSG8-MA21* [20] | *SG8* | *MA21* |
| *CMA21* [20] | *MA21* | *MA21* |
| **UDR Filters** | $W_1$ | $W_2$ |
| *UDR* [19] | 10 | N/A |
| *CUDR* | 10 | 25 |
| *CTUDR* | 5 | 20 |

the input $I(t)$ and the smoothed signal $Y(t)$, the result after applying the smoothing filter to $X(t)$, are calculated to evaluate the effectiveness of the proposed algorithm compared to other algorithms. The lower the *RMSE*, the better the performance of the smoothing filter, and vice versa, the higher the *COR*, the more algorithm effectiveness.

To evaluate the performance of a well-known classification model, EEGNet, on EEG data with and without applying smoothing algorithms, the Accuracy ($Acc$), $F1$-score, Precision ($Pr$), and Recall ($Rc$) are employed. Let $TP$, $TN$, $FP$, and $FN$ be the true positive, true negative, false positive, and false negative. The $Pr$, $Rc$, $Acc$, and $F1$-score are calculated as:

$$Pr = \frac{TP}{TP + FP}, \tag{19}$$

$$Rc = \frac{TP}{TP + FN}, \tag{20}$$

$$Acc = \frac{TP + TN}{TP + TN + FP + FN}, \tag{21}$$

$$F_1 = \frac{2 \times Pr \times Rc}{Pr + Rc}. \tag{22}$$

## IV. RESULT

### A. Experiments on Simulated Data

*1) Comparative Algorithms:* The comparative filters used in this work are reported in Table I, including nine non-cascaded and 11 cascaded ones. The parameters of the participating filters are recommended in [8] and [20].

*2) Results on Simulated Data:* The average results of non-cascaded comparative algorithms, CUDR and CTUDR on the test dataset are reported in Table II, which has confirmed not only the notable performance of UDR compared to other single-stage filters but also the significant enhancement of its cascaded arrangements.

As reported in Table II, if disregarding CUDR, UDR returns better results than other filters at 4 out of 6 SNR levels. At SNR from $-1$ to 10 dB, UDR has an average *RMSE* greater than the second-best filter that works on the time domain from 0.88% at SNR $=$ 10dB to 9.6% at SNR $=$ 5 dB. The *COR* results comparing UDR to the next-best filter at these SNR levels are from 0.05% at SNR $=$ 10 dB to 0.73% at SNR $=$ 1 dB.

The vulnerability of UDR occurs at very noisy signals (SNR $=$ $-5$, $-10$ dB). The quantitative results in Table II indicate the difference between UDR and the best performed filters, the cascade variants of UDR, is $-0.5\%$ to $-10.27\%$ in *RMSE* and $-0.01\%$ to $-1.29\%$ in *COR*. As discussed, UDR is sensitive to noisy signal with low SNR levels. In these scenarios, CUDR and CTUDR have demonstrated their advantages. Table II shows the significant enhancement of CUDR over UDR at low SNRs ($-10$, $-5$, $-1$, and 1dB). At these SNR levels, compared to UDR results, CUDR enhances 3.03% to 38.34% in *RMSE* and 0.32% to 4.16% in *COR*. However, these results of CUDR did not happen at the higher SNRs (5 and 10dB) as UDR did. The difference between CUDR and UDR at those noise levels is $-8.32\%$ to $-2.9\%$ in *RMSE* and $-0.12\%$ to 0.03% in *COR*.

It is significant to see that CUDR performs better than UDR at low SNRs but not at higher SNRs. Among the proposed cascaded variants of UDR, the performance of CTUDR is more significant at all SNRs. Indeed, the difference between CTUDR and UDR in *RMSE* is from 0.83% to 35.51% and 0.02% to 3.99% in *COR*. The highest enhancement of CTUDR to UDR is in very noisy signals where SNR $=$ $-10$ dB. These results indicate that CTUDR is the best cascaded variants of UDR at all noisy levels. Compared to CUDR, CTUDR has better results in 5 of 6 levels, reducing *RMSE* from 2.89% to 9.15% and increasing *COR* from 0.14% to 0.32% at SNR $=$ $-5$, $-1$, 1, 5, and 10dB. Although at SNR $=$ $-10$dB where CUDR has the best results, CTUDR is ranked the second-best, outperforming the remaining participating filters. The performance of CTUDR demonstrates its signal smoothing ability in both low and high SNRs, while CUDR is only effective at the former.

Table III shows the comparison between cascaded smoothing algorithms. Regardless of the results of CTUDR, CUDR outruns the remaining ones in 5 of 6 SNR levels. Notably, at SNR $=$ $-10$, $-5$, $-1$, 1, and 5dB, CUDR is better than the next-best from 2.89% to 9.65% in *RMSE* and 0.54% to 1.45% in *COR*. However, at SNR $=$ 10dB, the limitation of CURD at high level SNR signal is more obvious. On the other hand, although CTUDR only has the best results at 4 of 6 levels of noise, its performance at the remaining two is ranked the second-best. This result indicates the robustness of CTUDR at various noise levels. In this experiment, a disk-shaped structuring element is employed in the skeleton dilation with a radius of 20.

### B. Experiments on Real Data

In this experiment, the effectiveness of the proposed UDR variants and participating filters is verified by evaluating the

TABLE II
AVERAGE RESULTS OF COMPARATIVE NON-CASCADED AND PROPOSED ALGORITHMS ON TEST SIGNALS

| Signal | *SNR* | Metrics | *MA5* | *MA15* | *SG2* | *SG4* | *MF* | *BF* | *SG8* | *MA21* | *UDR* | *CUDR* | *CTUDR* |
|---|---|---|---|---|---|---|---|---|---|---|---|---|---|
| Simulated | -10 | RMSE | 4.5147 | 2.6330 | 7.0334 | 3.6546 | 4.1138 | 3.5749 | 5.5188 | 2.2640 | 2.3667 | **1.9833** | 2.0116 |
| | | COR | 0.5766 | 0.7681 | 0.4130 | 0.6575 | 0.6122 | 0.6595 | 0.5004 | 0.8103 | 0.7974 | **0.8390** | 0.8373 |
| | -5 | RMSE | 2.5412 | 1.5140 | 3.9552 | 2.0557 | 2.3145 | 2.0643 | 3.1036 | 1.3462 | 1.3512 | 1.1819 | **1.1530** |
| | | COR | 0.7818 | 0.9018 | 0.6278 | 0.8406 | 0.8091 | 0.8354 | 0.7168 | 0.9188 | 0.9187 | 0.9350 | **0.9372** |
| | -1 | RMSE | 1.0000 | 1.0001 | 2.4957 | 1.2977 | 1.4613 | 1.3748 | 1.9584 | 0.9432 | 0.8827 | 0.8152 | **0.7514** |
| | | COR | 0.8930 | 0.9534 | 0.7877 | 0.9263 | 0.9090 | 0.9160 | 0.8523 | 0.9577 | 0.9634 | 0.9692 | **0.9724** |
| | 1 | RMSE | 1.2787 | 0.8275 | 1.9824 | 1.0314 | 1.1613 | 1.1450 | 1.5558 | 0.8151 | 0.7234 | 0.6931 | **0.6145** |
| | | COR | 0.9281 | 0.9674 | 0.8494 | 0.9515 | 0.9396 | 0.9395 | 0.8989 | 0.9679 | 0.9752 | 0.9784 | **0.9815** |
| | 5 | RMSE | 0.8132 | 0.6001 | 1.2510 | 0.6522 | 0.7335 | 0.8457 | 0.9820 | 0.6576 | 0.5041 | 0.5331 | **0.4366** |
| | | COR | 0.9690 | 0.9825 | 0.9310 | 0.9797 | 0.9745 | 0.9657 | 0.9558 | 0.9788 | 0.9881 | 0.9884 | **0.9908** |
| | 10 | RMSE | 0.4698 | 0.4617 | 0.7038 | 0.3696 | 0.4136 | 0.6676 | 0.5530 | 0.5722 | 0.3607 | 0.4439 | **0.3524** |
| | | COR | 0.9893 | 0.9895 | 0.9765 | 0.9934 | 0.9917 | 0.9782 | 0.9853 | 0.9839 | 0.9939 | 0.9927 | **0.9941** |

TABLE III
AVERAGE RESULTS OF COMPARATIVE CASCADED ALGORITHMS ON TEST SIGNALS

| Signal | *SNR* | Metrics | *CMA5* | *CMA15* | *CSG2* | *CSG4* | *CMF* | *CSG8-BF* | *CSG8* | *CSG8-MA21* | *CMA21* | *CUDR* | *CTUDR* |
|---|---|---|---|---|---|---|---|---|---|---|---|---|---|
| Simulated | -10 | RMSE | 3.7288 | 2.2504 | 6.3489 | 3.3384 | 3.6115 | 3.5622 | 5.1858 | 2.2299 | 2.0655 | **1.9833** | 2.0116 |
| | | COR | 0.6487 | 0.8086 | 0.4490 | 0.6908 | 0.6613 | 0.6608 | 0.5239 | 0.8145 | 0.8245 | **0.8390** | 0.8373 |
| | -5 | RMSE | 2.1061 | 1.4019 | 3.5703 | 1.8779 | 2.0329 | 2.0574 | 2.9164 | 1.3281 | 1.4340 | 1.1819 | **1.1530** |
| | | COR | 0.8337 | 0.9111 | 0.6663 | 0.8618 | 0.8429 | 0.8363 | 0.7381 | 0.9207 | 0.9036 | 0.9350 | **0.9372** |
| | -1 | RMSE | 1.3416 | 1.0499 | 2.2528 | 1.1856 | 1.2847 | 1.3706 | 1.8403 | 0.9329 | 1.2004 | 0.8152 | **0.7514** |
| | | COR | 0.9214 | 0.9473 | 0.8169 | 0.9374 | 0.9274 | 0.9165 | 0.8663 | 0.9585 | 0.9299 | 0.9692 | **0.9724** |
| | 1 | RMSE | 1.0753 | 0.9443 | 1.7895 | 0.9424 | 1.0218 | 1.1419 | 1.4620 | 0.8076 | 1.1361 | 0.6931 | **0.6145** |
| | | COR | 0.9473 | 0.9568 | 0.8722 | 0.9590 | 0.9522 | 0.9398 | 0.9091 | 0.9685 | 0.9367 | 0.9784 | **0.9815** |
| | 5 | RMSE | 0.7030 | 0.8215 | 1.1293 | 0.5962 | 0.6473 | 0.8440 | 0.9229 | 0.6539 | 1.0658 | 0.5331 | **0.4366** |
| | | COR | 0.9764 | 0.9669 | 0.9427 | 0.9830 | 0.9800 | 0.9658 | 0.9606 | 0.9790 | 0.9439 | 0.9884 | **0.9908** |
| | 10 | RMSE | 0.4411 | 0.7594 | 0.6354 | **0.3384** | 0.3683 | 0.6669 | 0.5198 | 0.5710 | 1.0325 | 0.4439 | 0.3524 |
| | | COR | 0.9905 | 0.9716 | 0.9808 | **0.9944** | 0.9934 | 0.9783 | 0.9870 | 0.9839 | 0.9472 | 0.9927 | 0.9941 |

performance of EEGNet on the CC data, with and without a filter. EEGNet is employed on the raw data, and the data that has been smoothed by the participating filters, the 5-fold cross-validation of which is reported in Table IV.

Let $W_x$, $W_y$, and SE be respectively the linewidth in two stages of UDR-based filters and the structuring element for dilation in CTUDR. Then, UDR$W_x$ is the UDR using linewidth $x$, CUDR$W_xW_y$ is the cascaded arrangement of UDR$W_x$ and UDR$W_y$, and CTUDR$W_xW_y$SE is CTUDR which starts with UDRW$W_x$ being cascaded with the thinning process using image dilation with $W_y$ and SE. As reported in Table IV, the performance of EEGNet on datasets filtered by UDR-based techniques are better than on the non-filtered ones except the one modified by CUDR. Here, the MA variants and SG821 are verified to be able to improve the performance of EEGNet on the smoothed data. However, the improvements of EEGNet in terms of *Acc*, *Pr*, and $F_1$ on datasets filtered with those techniques do not exceed 0.5%. On the other hand, the improvements of EEGNet on datasets filtered by two CTUDR variants with different SEs are more significant. Notably, CTUDR with diamond structure-based dilation has improved the EEGNet performance by over 0.7% in all evaluation metrics compared to that on the raw data.

The processing time of participating filters is reported in Table V. Despite the effectiveness of UDR-based filters on simulated and EEG signals, their processing time is still higher than that of the counterparts. Due to the image domain-based mechanism, image processing techniques are required, resulting in a accuracy-complexity trade-off. As demonstrated in Table V, the processing time of CTUDR is approximately 38.4% and 63.7% of that of CUDR, although more optimization is required to be comparable to their time-domain counterparts.

Fig. 5 visualizes the 5-fold cross-validation results of EEGNet on the cognitive conflict data, with and without UDR-based filters. In general, the results of EEGNet on data smoothed by UDR-based filters are higher than that on the raw data in most of the folds. Indeed, *Acc* and $F_1$ of EEGNet on the filtered data with UDR-based filters are better in all folds. Notably, in terms of *Acc*, $F_1$, and *Pr* metrics, performance of EEGNet on the data filtered by CTUDR has better results in at least 60% of the folds. These results also confirm the classification stability of EEGNet on the data filtered by UDR reported in [19] when the standard deviation of *Acc* and $F_1$ (1.02% and 0.95%, respectively) is lower than that on the non-filtered data (1.08% and 1.18%, respectively). Inheriting the stability when using UDR, the standard deviation of all evaluation metrics of EEGNet on the data smoothed by CTUDR is lower than on the raw one. Notably, performance of EEGNet on the CTUDR-filtered dataset is even more stable than using UDR in all evaluation metrics except in the standard deviation of the $F_1$. Contrary to the results of CUDR on simulated signals, the performance of EEGNet on the data using this filter is not that impressive. However, as shown in Fig 5, the results on the CUDR-filtered data are also higher than those on the non-smoothed data on 3 out of 5 folds.

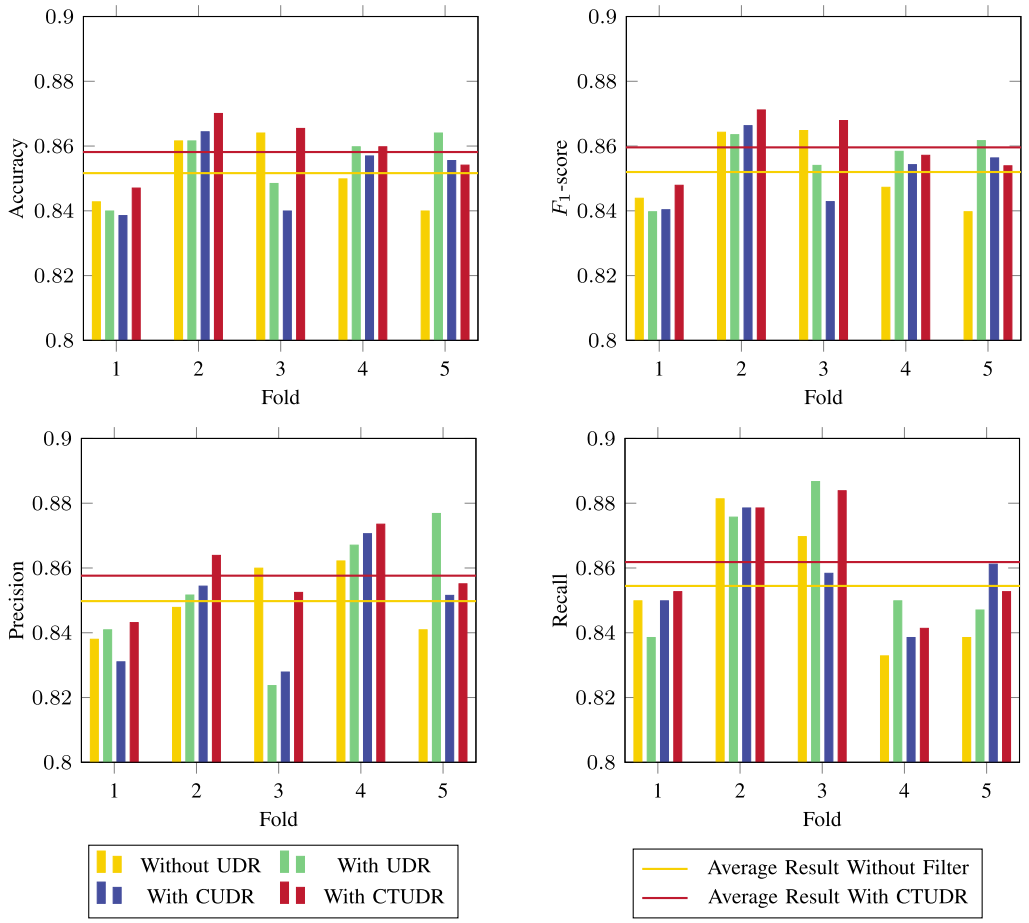


Fig. 5. 5-fold cross evaluation results of EEGNet, with and without UDR-based filters.

These experiments were performed on an Intel(R) Core(TM) i9-10900 CPU @2.80GHz with 64GB RAM and GPU NVIDIA GeForce GTX 3090 using MATLAB R2021b for Ubuntu 20.04.5 LTS.

## V. Parameters Analysis

In this section, the parameters of the morphological opening and the second dilation are fine-tuned to analyze their effect on CTUDR performance. First, the parameters of the morphological opening are fixed with a disk-shaped of radius 2 and 4 for erosion and dilation, while the second dilation is fine-tuned. According to our observation and analysis, the signal peak have half ellipse or round wave shapes, even when being visualized in binary images. To reduce the branches corresponding to noise while still keeping the signal structure the disk-shape structuring element is selected in the erosion with the radius of 2. The radius is initially kept at a small value to preserve the signal structure while evaluating the effectiveness of different structuring elements in the second dilation. To ensure the plotted signal is not damaged much by the erosion, the same structuring element is employed in the first dilation with a radius of 4.

The existing structuring elements in MATLAB employed for the fine-tuning is presented in Table VI. The best results of those structures with their optimized parameters are reported in Table VII. These results have verified the great potential of image dilation to replace the visualization step in the cascaded stage as per the CUDR. This image-processing-based technique also enhances the quality of signal smoothing, reduces the processing time, and provides a variety of structures to optimize the final result. It could be seen that the results are significantly enhanced from 3.51% to 16.71% in *RMSE* and 0.19% to 2.11% in *COR* compared to CTUDR using disk structure for the second dilation with radius = 20 reported in Table III.

Next, the parameters of the second dilation in CTUDR are fixed following the results in Table VII to keep the best dilation performance in the cascaded stage. Then, the parameter set of the morphological opening is fine-tuned with all options reported in Table VI, the results of which are shown in Table VIII. It is significant to see that the performance of CTUDR is even more improved when modifying the parameters of the morphological opening. More importantly, the *RMSE* results increase in the range of 0.68% to 16.75% and 0.02% to 1.99% in *COR* compared to CTUDR with the fine-tuned second dilation only. These results indicate the effectiveness when using a suitable parameter set for the morphological opening in CTUDR.

Notably, there are only a few structures (disk, diamond, and octagon) for the opening operators that could enhance the CTUDR smoothing ability, while every structure in the second dilation could improve CTUDR performance. As the signal

TABLE IV
PERFORMANCE OF EEGNET ON CC UNDER THE IMPACT OF SMOOTHING FILTERS

| Filters | Accuracy | Precision | Recall | F-measure |
|---|---|---|---|---|
| W/o filter | 85.1637% | 84.9768% | 85.4458% | 85.1983% |
| **Non-cascaded filters** | | | | |
| BF | 85.1640% | 84.8776% | 85.6159% | 85.2268% |
| MA5 | 85.5321% | 85.1631% | 86.1257% | 85.6180% |
| MA15 | 85.3340% | 84.7659% | 86.1824% | 85.4557% |
| MA21 | 85.4185% | 85.1110% | 85.8984% | 85.4812% |
| SG25 | 85.2205% | 84.5346% | 86.2387% | 85.3640% |
| SG427 | 85.1355% | 84.3854% | 86.2390% | 85.2936% |
| SG821 | 85.3622% | 84.6553% | 86.4087% | 85.5104% |
| MF | 85.1071% | 84.6635% | 85.7856% | 85.1948% |
| **Cascaded filters** | | | | |
| CSG8-BF | 85.1640% | 84.8776% | 85.6159% | 85.2268% |
| CMA5 | 85.6166% | 85.2977% | 86.1255% | 85.6869% |
| CMA15 | 85.4472% | 85.3342% | 85.6723% | 85.4780% |
| CMA21 | 85.5606% | 84.9825% | **86.4093%** | 85.6775% |
| CSG25 | 85.2489% | 84.5831% | 86.2387% | 85.3880% |
| CSG427 | 85.0788% | 84.4067% | 86.0690% | 85.2180% |
| CSG821 | 85.3622% | 84.6553% | 86.4087% | 85.5104% |
| CMF | 85.1071% | 84.6635% | 85.7856% | 85.1948% |
| CSG8-MA21 | 85.2490% | 84.9869% | 85.6724% | 85.3089% |
| **UDR-based filters** | | | | |
| UDR_25 | 85.4753% | 85.2025% | 85.9561% | 85.5458% |
| CUDR(5, 20) | 84.6826% | 84.7544% | 84.6531% | 84.6759% |
| CUDR(10, 25) | 85.1068% | 84.7084% | 85.7293% | 85.2013% |
| CTUDR(5, 20) disk | 85.8153% | 85.4264% | 86.4088% | 85.8959% |
| CTUDR(5, 20) diamond | **85.9280%** | **85.7626%** | 86.1825% | **85.9590%** |

peaks appear with a half-disk shape, the opening techniques work well with the element structures of similar appearance. The goal of the opening operators is noise reduction by removing unwanted parts and regenerating the missing ones; hence it is crucial to preserve the structure during the progress to avoid changing the form of the original signal. Meanwhile, the second dilation's goal is to smooth the skeleton and has no impact on the skeleton's structure, explaining the suitability of all element shapes in the enhancement of CTUDR in the second dilation.

## VI. DISCUSSION

The experiment results in this work have confirmed the performance of the UDR filter family and emphasized the promising potential of the proposed CTUDR in signal smoothing. Compared to its non-cascaded counterparts, UDR returns smaller fitting errors on test signals with SNR ranging in $[-1, 10]$. CUDR, on the other hand, shows a better signal correlation on the simulated data compared to the non-cascaded and cascaded arrangements of conventional filters. Last but most importantly, CTUDR demonstrates its superior performance, especially on distorted signals with SNR ranging in $[-5, 5]$. At SNR of $-10$ dB and 10dB, CTUDR is the second best, while the corresponding best filter is CUDR and CSG4. The results of the signal smoothing task have also confirmed the improved performance of the cascaded arrangement of all participating filters against their non-cascaded one.

TABLE V
PROCESSING TIME OF COMPARATIVE ALGORITHMS

| Signal | Algorithms | Duration (ms) | Sampling rate (Hz) | Processing time (ms) |
|---|---|---|---|---|
| Simulated | BF | 25000 | 1000 | 0.726 |
| | MA5 | | | 0.302 |
| | MA15 | | | 0.244 |
| | MA21 | | | 0.289 |
| | SG25 | | | 0.300 |
| | SG427 | | | 0.328 |
| | SG821 | | | 0.371 |
| | MF | | | 2.140 |
| | CSG8-BF | | | 1.000 |
| | CMA5 | | | 0.245 |
| | CMA15 | | | 0.408 |
| | CMA21 | | | 0.378 |
| | CSG25 | | | 0.498 |
| | CSG427 | | | 0.592 |
| | CSG821 | | | 0.577 |
| | CMF | | | 3.683 |
| | CSG8-MA21 | | | 0.769 |
| | UDR | | | 507.051 |
| | CUDR | | | 2080.902 |
| | CTUDR | | | 798.072 |
| EEG | BF | 1000 | 1200 | 0.099 |
| | MA5 | | | 0.048 |
| | MA15 | | | 0.038 |
| | MA21 | | | 0.042 |
| | SG25 | | | 0.127 |
| | SG427 | | | 0.102 |
| | SG821 | | | 0.097 |
| | MF | | | 0.181 |
| | CSG8-BF | | | 0.146 |
| | CMA5 | | | 0.049 |
| | CMA15 | | | 0.047 |
| | CMA21 | | | 0.048 |
| | CSG25 | | | 0.128 |
| | CSG427 | | | 0.144 |
| | CSG821 | | | 0.199 |
| | CMF | | | 0.156 |
| | CSG8-MA21 | | | 0.199 |
| | UDR | | | 174.702 |
| | CUDR | | | 356.245 |
| | CTUDR | | | 227.391 |

Due to its mechanism, more operations are executed in a cascaded arrangement compared to the non-cascaded one, leading to higher processing time as shown in Table V. For CUDR, this computational cost is even elevated since an extra time-image domain transformation is required. The development of CTUDR allows bypassing the second binary image representation, hence reducing the runtime. The novelty here lies in the leverage of morphology operations, i.e. erosion, dilation, and opening, providing a similar result in a shorter duration. Although CTUDR is 2.6 and 1.6 times faster than CUDR in the signal smoothing and classification task, representing signals at higher line width levels is a foreseen computational cost challenge.

In the classification task, performances of EEGNet on datasets filtered with two different CTUDRs are respectively 0.6516% and 0.7643% better than on the non-filtered data in terms of $Acc$. The reason that has led to the out-performance of the cascaded UDR filters is the cascaded arrangement with

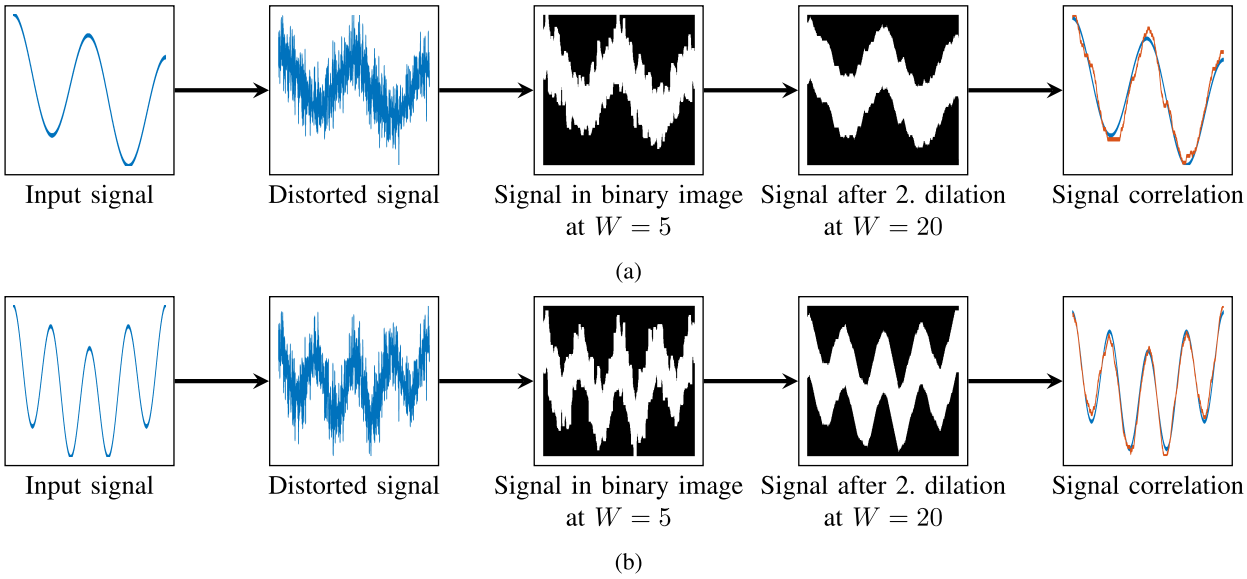


Fig. 6. Impact of signal frequencies on CTUDR: (a) low-frequency signal, (b) high-frequency signal.

TABLE VI
FINE-TUNING OF MORPHOLOGICAL STRUCTURING ELEMENTS IN CTUDR

| **Erosion** | | |
|---|---|---|
| SE | Radius/Length | Degree/Length |
| Diamond | 1 to 5 step 1 | N/A |
| Disk | 1 to 5 step 1 | N/A |
| Octagon | 3 to 6 step 3 | N/A |
| Square | 1 to 5 step 1 | N/A |
| Line | 1 to 5 step 1 | 45, 90, 135, 180 degree |
| Rectangle | 1 to 5 step 1 | 1 to 5 step 1 |
| **First Dilation** | | |
| SE | Radius/Length | Degree/Length |
| Diamond | 1 to 7 step 1 | N/A |
| Disk | 1 to 7 step 1 | N/A |
| Octagon | 3 to 9 step 3 | N/A |
| Square | 1 to 7 step 1 | N/A |
| Line | 1 to 7 step 1 | 45, 90, 135, 180 degree |
| Rectangle | 1 to 7 step 1 | 1 to 7 step 1 |
| **Second Dilation** | | |
| SE | Radius/Length | Degree/Length |
| Diamond | 5 to 30 step 5 | N/A |
| Disk | 5 to 30 step 5 | N/A |
| Octagon | 3 to 33 step 6 | N/A |
| Square | 5 to 30 step 5 | N/A |
| Line | 5 to 30 step 5 | 45, 90, 135, 180 degree |
| Rectangle | 5 to 30 step 5 | 5 to 30 step 5 |

TABLE VII
AVERAGE RESULTS OF CTUDR USING DIFFERENTS STRUCTURES IN THE SECOND DILATION ON TEST SIGNALS

| SNR | Structure | Radius | Degree/Length | RMSE | COR |
|---|---|---|---|---|---|
| -10 | Diamond | 30 | N/A | **1.8445** | **0.8584** |
| | Disk | 30 | N/A | 1.9263 | 0.8458 |
| | Octagon | 33 | N/A | 1.8922 | 0.8505 |
| | Square | 30 | N/A | 1.8533 | 0.8549 |
| | Line | 30 | 180 | 1.9007 | 0.8476 |
| | Rectangle | 10 | 30 | 1.8855 | 0.8498 |
| -5 | Diamond | 30 | N/A | **1.0612** | **0.9468** |
| | Disk | 30 | N/A | 1.1153 | 0.9406 |
| | Octagon | 33 | N/A | 1.1235 | 0.9404 |
| | Square | 30 | N/A | 1.0769 | 0.9440 |
| | Line | 30 | 180 | 1.0823 | 0.9431 |
| | Rectangle | 20 | 30 | 1.0734 | 0.9442 |
| -1 | Diamond | 30 | N/A | **0.7024** | **0.9764** |
| | Disk | 25 | N/A | 0.7319 | 0.9740 |
| | Octagon | 33 | N/A | 0.7773 | 0.9714 |
| | Square | 30 | N/A | 0.7133 | 0.9750 |
| | Line | 30 | 180 | 0.7214 | 0.9752 |
| | Rectangle | 10 | 25 | 0.7079 | 0.9753 |
| 1 | Diamond | 30 | N/A | 0.5863 | 0.9838 |
| | Disk | 25 | N/A | 0.6034 | 0.9826 |
| | Octagon | 27 | N/A | 0.6523 | 0.9801 |
| | Square | 30 | N/A | 0.5903 | 0.9830 |
| | Line | 25 | 180 | 0.5892 | 0.9836 |
| | Rectangle | 20 | 25 | **0.5821** | **0.9834** |
| 5 | Diamond | 20 | N/A | 0.4220 | 0.9918 |
| | Disk | 15 | N/A | 0.4362 | 0.9912 |
| | Octagon | 15 | N/A | 0.4706 | 0.9899 |
| | Square | 25 | N/A | 0.4143 | 0.9920 |
| | Line | 15 | 180 | 0.4249 | 0.9915 |
| | Rectangle | 20 | 25 | **0.4015** | **0.9923** |
| 10 | Diamond | 15 | N/A | 0.2898 | 0.9962 |
| | Disk | 5 | N/A | 0.3017 | 0.9956 |
| | Octagon | 9 | N/A | 0.3227 | 0.9954 |
| | Square | 15 | N/A | 0.2915 | 0.9961 |
| | Line | 25 | 90 | 0.2977 | 0.9959 |
| | Rectangle | 10 | 15 | **0.2797** | **0.9962** |

two different line width values at each stage to take advantage of the original UDR while overcoming its limitation. When the noisy signal is plotted with a small line width at the first stage, the waveform of the original signal is preserved. Then, at the cascaded stage using a higher line width, the immediate result is smoothed, outputting the filtered signal with a high correlation to the original one.

Fig. 6(a) and Fig. 6(b) illustrate the performance variance of CTUDR across two signal segments in the same duration, using a test sample of signal 4 and signal 3 at SNR = 1dB, respectively. Notably, even when dealing with higher-frequency signals, CTUDR demonstrates effectiveness by maintaining the waveform while reducing the minor peaks. This characteristic could be valuable for eliminating

TABLE VIII
AVERAGE RESULTS OF CTUDR USING DIFFERENTS STRUCTURES IN THE OPENING TECHNIQUES ON TEST SIGNALS

| SNR | Erosion | Dilation | RMSE | COR |
|---|---|---|---|---|
| -10 | Diamond-5 | Diamond-7 | 1.7308 | 0.8729 |
| | Disk-5 | Disk-7 | 1.6830 | 0.8770 |
| | Octagon-6 | Octagon-9 | **1.6770** | **0.8783** |
| | Square-5 | Square-7 | 1.9102 | 0.8505 |
| | Line-1,90 | Line-3,90 | 1.8858 | 0.8522 |
| | Rectangle-2,1 | Rectangle-4,3 | 1.9099 | 0.8507 |
| -5 | Diamond-5 | Diamond-7 | 1.0046 | 0.9522 |
| | Disk-5 | Disk-7 | 0.9866 | 0.9537 |
| | Octagon-6 | Octagon-9 | **0.9832** | **0.9542** |
| | Square-5 | Square-7 | 1.0958 | 0.9435 |
| | Line-1,90 | Line-3,90 | 1.0805 | 0.9443 |
| | Rectangle-2,1 | Rectangle-4,3 | 1.0940 | 0.9436 |
| -1 | Diamond-5 | Diamond-7 | 0.6766 | 0.9783 |
| | Disk-5 | Disk-7 | 0.6694 | 0.9789 |
| | Octagon-6 | Octagon-9 | **0.6665** | **0.9791** |
| | Square-5 | Square-7 | 0.7236 | 0.9750 |
| | Line-1,90 | Line-3,90 | 0.7099 | 0.9755 |
| | Rectangle-2,1 | Rectangle-4,3 | 0.7221 | 0.9750 |
| 1 | Diamond-5 | Diamond-7 | 0.5611 | 0.9846 |
| | Disk-5 | Disk-7 | **0.5562** | **0.9850** |
| | Octagon-6 | Octagon-9 | 0.6026 | 0.9828 |
| | Square-5 | Square-7 | 0.6044 | 0.9821 |
| | Line-1,90 | Line-3,90 | 0.6041 | 0.9824 |
| | Rectangle-5,1 | Rectangle-7,3 | 0.6044 | 0.9821 |
| 5 | Diamond-5 | Diamond-7 | 0.3930 | 0.9927 |
| | Disk-5 | Disk-7 | **0.3925** | **0.9928** |
| | Octagon-6 | Octagon-9 | 0.3917 | 0.9928 |
| | Square-5 | Square-7 | 0.4346 | 0.9909 |
| | Line-2,90 | Line-4,90 | 0.4310 | 0.9911 |
| | Rectangle-5,1 | Rectangle-7,3 | 0.4343 | 0.9909 |
| 10 | Diamond-5 | Diamond-7 | 0.2732 | 0.9964 |
| | Disk-5 | Disk-7 | **0.2729** | **0.9964** |
| | Octagon-6 | Octagon-9 | 0.3419 | 0.9940 |
| | Square-5 | Square-7 | 0.3658 | 0.9932 |
| | Line-2,90 | Line-4,90 | 0.3642 | 0.9932 |
| | Rectangle-5,1 | Rectangle-7,3 | 0.3653 | 0.9932 |

high-frequency noises like muscular artifacts, which will be explored further in our future research. Fig. 6 also shows a potential limitation: when processing high-frequency signals, dominant peaks might be represented by overlapped white pixels and disappear when being skeletonized. Although widening the binary image could solve the problem, it adds to the processing time because of the increased pixel number.

In summary, despite promising results in signal smoothing and classification for cognitive conflict analysis, there are rooms for improvement we would like to address in our future work:

- The trade-off between the computational cost and the data visualization, especially for high-frequency signals.
- The robustness of the current parameter setting on some particular artifacts.
- The impact of CTUDR on some specific morphologies and frequencies and their corresponding clinical significance.
- The feasibility of embedding CTUDR in a deep neural network for signal classification.

## VII. CONCLUSION

This paper introduces a cascaded thinning arrangement within the upscale and downscale representation scheme for EEG signal processing. Compared to our preliminary work, CUDR, the proposed CTUDR approach is faster and more effective in signal smoothing and classification tasks. The improvement in computational efficiency is derived from the refined processing pipeline, where the scale-changing stages are packed within one binary image representation. The notable enhancement when using some traditional morphological operations, as demonstrated in CTUDR, has shown potential for employing image processing techniques in signal processing. Besides optimizing the binary image representation, the feasibility of vision-based classification models in EEG signal processing as well as their applications in transient analysis will be investigated in our future study.

## ACKNOWLEDGMENT

The authors would like to thank Dr. Thuy Pham for her advice during the research phases. The computing facilities was supported in part by the Joint Technology and Innovation Research Centre (JTIRC), a partnership between the University of Technology Sydney and the VNU University of Engineering and Technology.

## REFERENCES

[1] F. A. Alturki, K. AlSharabi, A. M. Abdurraqeeb, and M. Aljalal, "EEG signal analysis for diagnosing neurological disorders using discrete wavelet transform and intelligent techniques," *Sensors*, vol. 20, no. 9, p. 2505, Apr. 2020.

[2] D. M. Praveena, D. A. Sarah, and S. T. George, "Deep learning techniques for EEG signal applications—A review," *IETE J. Res.*, vol. 68, no. 4, pp. 3030–3037, 2022.

[3] M.-P. Hosseini, A. Hosseini, and K. Ahi, "A review on machine learning for EEG signal processing in bioengineering," *IEEE Rev. Biomed. Eng.*, vol. 14, pp. 204–218, 2020.

[4] X. Gu et al., "EEG-based brain-computer interfaces (BCIs): A survey of recent studies on signal sensing technologies and computational intelligence approaches and their applications," *IEEE/ACM Trans. Comput. Biol. Bioinf.*, vol. 18, no. 5, pp. 1645–1666, Sep. 2021.

[5] W. O. Tatum IV, *Handbook of EEG Interpretation*. Cham, Switzerland: Springer, 2021.

[6] S. I. Alzahrani and M. M. Alsaleh, "The influence of smoothing filtering methods on the performance of an EEG-based brain–computer interface," *IEEE Access*, vol. 11, pp. 60171–60180, 2023.

[7] A. Chaddad, Y. Wu, R. Kateb, and A. Bouridane, "Electroencephalography signal processing: A comprehensive review and analysis of methods and techniques," *Sensors*, vol. 23, no. 14, p. 6434, Jul. 2023.

[8] A. Kawala-Sterniuk et al., "Comparison of smoothing filters in analysis of EEG data for the medical diagnostics purposes," *Sensors*, vol. 20, no. 3, p. 807, Feb. 2020.

[9] A. K. Roonizi and C. Jutten, "Band-stop smoothing filter design," *IEEE Trans. Signal Process.*, vol. 69, pp. 1797–1810, 2021.

[10] X. Su et al., "A comprehensive survey on community detection with deep learning," *IEEE Trans. Neural Netw. Learn. Syst.*, vol. 35, no. 4, pp. 4682–4702, Apr. 2024, doi: 10.1109/TNNLS.2021.3137396.

[11] T. H. Dinh, M. D. Phung, and Q. P. Ha, "Summit navigator: A novel approach for local maxima extraction," *IEEE Trans. Image Process.*, vol. 29, pp. 551–564, 2020.

[12] A. K. Roonizi, "A new approach to ARMAX signals smoothing: Application to variable-Q ARMA filter design," *IEEE Trans. Signal Process.*, vol. 67, no. 17, pp. 4535–4544, Sep. 2019.

[13] E. Perez-Valero, M. A. Lopez-Gordo, and M. A. Vaquero-Blasco, "EEG-based multi-level stress classification with and without smoothing filter," *Biomed. Signal Process. Control*, vol. 69, Aug. 2021, Art. no. 102881.

[14] A. Bhattacharyya, R. K. Tripathy, L. Garg, and R. B. Pachori, "A novel multivariate-multiscale approach for computing EEG spectral and temporal complexity for human emotion recognition," *IEEE Sensors J.*, vol. 21, no. 3, pp. 3579–3591, Feb. 2021.

[15] X. Hu, S. Yuan, F. Xu, Y. Leng, K. Yuan, and Q. Yuan, "Scalp EEG classification using deep bi-LSTM network for seizure detection," *Comput. Biol. Med.*, vol. 124, Sep. 2020, Art. no. 103919.

[16] Y. C. Yoon, "LIF and simplified SRM neurons encode signals into spikes via a form of asynchronous pulse sigma–delta modulation," *IEEE Trans. Neural Netw. Learn. Syst.*, vol. 28, no. 5, pp. 1192–1205, May 2017.

[17] A. Savitzky and M. J. E. Golay, "Smoothing and differentiation of data by simplified least squares procedures," *Anal. Chem.*, vol. 36, no. 8, pp. 1627–1639, Jul. 1964.

[18] M. Aubury and W. Luk, "Binomial filters," *J. VLSI Signal Process. Syst. Signal Image Video Technol.*, vol. 12, pp. 35–50, Jan. 1996.

[19] T. H. Dinh, A. K. Singh, Q. M. Doan, N. L. Trung, D. N. Nguyen, and C.-T. Lin. (2023). *An EEG Signal Smoothing Algorithm Using Upscale and Downscale Representation*. [Online]. Available: http://eprints.uet.vnu.edu.vn/eprints/id/eprint/4792

[20] S. Agarwal, A. Rani, V. Singh, and A. P. Mittal, "EEG signal enhancement using cascaded S-Golay filter," *Biomed. Signal Process. Control*, vol. 36, pp. 194–204, Jul. 2017.

[21] A. Saadia and A. Rashdi, "Fractional order integration and fuzzy logic based filter for denoising of echocardiographic image," *Comput. Methods Programs Biomed.*, vol. 137, pp. 65–75, Dec. 2016.

[22] T. Liu and D. Yao, "Removal of the ocular artifacts from EEG data using a cascaded spatio-temporal processing," *Comput. Methods Programs Biomed.*, vol. 83, no. 2, pp. 95–103, Aug. 2006.

[23] M. A. Islam, I. Bandyopadhyaya, P. Bhattacharyya, and G. Saha, "Multichannel lung sound analysis for asthma detection," *Comput. Methods Programs Biomed.*, vol. 159, pp. 111–123, Jun. 2018.

[24] G. Chen, Z. Hong, Y. Guo, and C. Pang, "A cascaded classifier for multi-lead ECG based on feature fusion," *Comput. Methods Programs Biomed.*, vol. 178, pp. 135–143, Sep. 2019.

[25] Q. M. Doan, T. H. Dinh, N. L. Trung, D. N. Nguyen, A. K. Singh, and C.-T. Lin, "Extended upscale and downscale representation with cascade arrangement," in *Proc. IEEE Stat. Signal Process. Workshop (SSP)*, Jul. 2023, pp. 715–719.

[26] A. K. Singh, H.-T. Chen, K. Gramann, and C.-T. Lin, "Intraindividual completion time modulates the prediction error negativity in a virtual 3-D object selection task," *IEEE Trans. Cognit. Develop. Syst.*, vol. 12, no. 2, pp. 354–360, Jun. 2020.

[27] A. K. Singh, K. Gramann, H.-T. Chen, and C.-T. Lin, "The impact of hand movement velocity on cognitive conflict processing in a 3D object selection task in virtual reality," *NeuroImage*, vol. 226, Feb. 2021, Art. no. 117578.

[28] M. J. Menten et al., "A skeletonization algorithm for gradient-based optimization," in *Proc. IEEE/CVF Int. Conf. Comput. Vis. (ICCV)*, vol. 17, Oct. 2023, pp. 21337–21346.

[29] T. C. Lee, R. L. Kashyap, and C. N. Chu, "Building skeleton models via 3-D medial surface axis thinning algorithms," *CVGIP, Graph. Models Image Process.*, vol. 56, no. 6, pp. 462–478, Nov. 1994.

[30] R. C. Gonzalez and R. E. Woods, *Digital Image Processing*. New York, NY, USA: Pearson, 2018.

[31] T. H. Dinh, A. K. Singh, N. Linh Trung, D. N. Nguyen, and C.-T. Lin, "EEG peak detection in cognitive conflict processing using summit navigator and clustering-based ranking," *IEEE Trans. Neural Syst. Rehabil. Eng.*, vol. 30, pp. 1548–1556, 2022.

[32] H. Azami and J. Escudero, "Amplitude-aware permutation entropy: Illustration in spike detection and signal segmentation," *Comput. Methods Programs Biomed.*, vol. 128, pp. 40–51, May 2016.

[33] A. K. Singh et al., "Visual appearance modulates prediction error in virtual reality," *IEEE Access*, vol. 6, pp. 24617–24624, 2018.

[34] V. J. Lawhern, A. J. Solon, N. R. Waytowich, S. M. Gordon, C. P. Hung, and B. J. Lance, "EEGNet: A compact convolutional neural network for EEG-based brain–computer interfaces," *J. Neural Eng.*, vol. 15, no. 5, Oct. 2018, Art. no. 056013.